



Soft EHL Simulations of Lubricant Film Thickness in Textured Hard-on-Soft Bearings Considering Different Cavitation Models, in the Context of Prosthetic Hip Implants

Quentin Allen¹ · Bart Raeymaekers¹

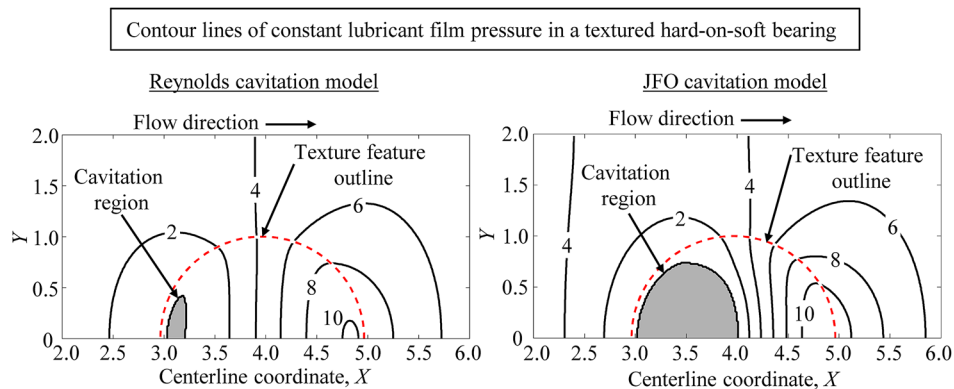
Received: 25 May 2021 / Accepted: 15 August 2021

© The Author(s), under exclusive licence to Springer Science+Business Media, LLC, part of Springer Nature 2021

Abstract

We use soft elasto-hydrodynamic lubrication simulations to calculate the lubricant film thickness in textured hard-on-soft parallel slider bearings and compare a mass-conserving cavitation model based on the Elrod implementation of the Jakobson, Floberg, and Olsson (JFO) theory to simplified Reynolds and half-Sommerfeld cavitation models. We determine the optimum texture design parameters that maximize the lubricant film thickness for a range of bearing operating conditions and compare the results obtained with the different cavitation models. We determine that the JFO cavitation model predicts smaller optimum texture aspect ratios than the Reynolds cavitation model, and that the difference between the lubricant film thickness calculated with the different cavitation models increases with increasing texture aspect ratio and decreasing flow factor. These results are useful to determine when the mass-conserving JFO cavitation model or the simplified Reynolds cavitation model should be employed. Furthermore, the results are relevant to designing textured hard-on-soft bearings with application in, e.g., prosthetic hip implants.

Graphic Abstract



Keywords Compliant surface EHL · Cavitation in hydrodynamics · Surface modification · Human joints · replacements · Lubricant film thickness

✉ Bart Raeymaekers
bart.raeymaekers@utah.edu

¹ Department of Mechanical Engineering, University of Utah, 1495 E. 100 S. (1550 MEK), Salt Lake City, UT 84112, USA

List of symbols

c	Bearing surface separation
$d(x,y)$	Polyethylene deformation
$D(X,Y)$	Non-dimensional polyethylene deformation, $d/2r_p$
E	Young's modulus
$h(x,y)$	Lubricant film thickness

$H(X, Y)$	Non-dimensional lubricant film thickness, h/c (simulation), or $h/2r_p$ (results)
H_{\min}	Minimum non-dimensional lubricant film thickness
H_{opt}	Optimum non-dimensional lubricant film thickness
h_p	Depth of texture feature
$p(x, y)$	Lubricant film pressure
$P(X, Y)$	Non-dimensional lubricant film pressure, p/p_0
p_0	Atmospheric pressure
P_{avg}	Average non-dimensional lubricant film pressure
P_{cav}	Cavitation threshold
P_{cav}	Non-dimensional cavitation threshold
r_l	Half-length of square unit cell
r_p	Radius of texture feature
S_p	Texture density, $\pi r_p^2/4r_l^2$
$S_{p \text{ max}}$	Maximum texture density, $\pi/4$
U	Relative sliding velocity between bearing surfaces
W	Bearing load-carrying capacity, $\iint P(X, Y) dXdY = P_{\text{avg}}$
x, y, z	Cartesian coordinates
X, Y, Z	Non-dimensional Cartesian coordinates, $x/r_p, y/r_p, z/r_p$
δ	Non-dimensional bearing surface separation, $c/2r_p$
ε	Texture aspect ratio, $h_p/2r_p$
ε_{opt}	Optimum texture aspect ratio
$\theta(X, Y)$	Fractional film content parameter
λ	Flow factor, $3\mu U/2r_p p_0$
μ	Dynamic viscosity
ν	Poisson's ratio

1 Introduction

Total hip replacement (THR) is one of the most successful surgeries performed in the United States (US) and replaces a patient's diseased or damaged hip joint with a prosthetic hip implant [1]. According to the most recent publicly available data from the National Inpatient Sample (NIS), more than 370,770 THR surgeries were performed in US hospitals in 2014, and 635,000 THR surgeries are predicted to occur annually by 2030 [2]. The increasing number of THR surgeries is driven by an aging population and increasing numbers of young patients seeking THR to maintain active lifestyles [3]. A prosthetic hip implant comprises a spherical femoral head, which attaches to the neck of a femoral stem that is anchored in the femur. The femoral head articulates with a hemispherical acetabular cup (or a shell with an acetabular liner) implanted in the pelvis, to replace the function of the natural hip joint [4].

Prosthetic hip implants are often categorized by their bearing material pairs, including metal-on-polyethylene (MoP), metal-on-metal (MoM), ceramic-on-polyethylene (CoP), and ceramic-on-ceramic (CoC). Presently, hard-on-soft (MoP, CoP) bearing material pairs represent almost 93% of new prosthetic hip implants and have a long history of clinical success [5]. It has been documented that hard-on-hard material pairs (MoM, CoC) may wear less than hard-on-soft material pairs [6], but they are prone to complications such as metal ion release (MoM) [7] or squeaking and fracture (CoC) [8]. In this paper, we specifically focus on hard-on-soft prosthetic hip implant material pairs.

The statistical survivorship of prosthetic hip implants declines after 15–25 years of use [9]. When a prosthetic hip implant fails, a revision surgery replaces a failed prosthetic hip implant with a new one. The NIS documents that the most common reasons for revision surgeries include mechanical complications (19%), dislocation (17%), mechanical loosening (15%), and infection (14%) [10]. Loosening and other complications commonly relate to osteolysis [11], which in hard-on-soft prosthetic hip implants, is caused by a biological reaction to microscopic ultra-high molecular weight polyethylene (UHMWPE) wear debris that weakens the bone and causes mechanical loosening and instability [12]. Hence, reducing polyethylene wear debris remains important to improving the longevity of hard-on-soft prosthetic hip implants.

Research to reduce polyethylene wear in MoP prosthetic hip implants focuses on improving the mechanical properties of the polyethylene liner and/or changing the design of the femoral head. Specifically, cross-linking UHMWPE has shown to increase strength and reduce wear with great clinical success [13]. However, it also increases oxidation and fatigue wear [14], which can be reduced using antioxidant additives such as vitamin-E [15, 16]. Furthermore, manufacturing the femoral head with ceramic instead of metallic materials increases hardness and enables reducing surface roughness. It also provides greater wettability, which improves lubricity [17]. Surface coatings such as diamond-like carbon, tantalum, or titanium nitride also increase hardness and reduce surface roughness of the femoral head [18].

Additionally, the literature documents that a pattern of texture features on prosthetic hip implant bearing surfaces can increase the lubricant film thickness and, thus, reduce friction and wear. For instance, pin-on-disk (PoD) [19–21], ring-on-disk (RoD) [22], ball-on-disk (BoD) [23], and hip joint simulators experiments [24] demonstrate that a pattern of texture features on the surfaces of hard-on-soft bearings can substantially reduce polyethylene wear [25]. Numerical elasto-hydrodynamic lubrication (EHL) simulations based on solving the Navier–Stokes (NS) or Reynolds equation (RE) also document the effect of texture design parameters and bearing operating conditions on, e.g., lubricant film

thickness [26], lubricant film pressure [27], and friction forces [28] within the bearing. Cavitation forms gas bubbles from dissolved gas or vapor in a liquid lubricant film when the lubricant film pressure locally decreases below the saturation or vapor pressure [29]. Different cavitation models have been used in numerical simulations of lubrication problems, including the half-Sommerfeld (HS), Reynolds, and Jakobsson–Floberg–Olsson (JFO) cavitation models, which differ in the boundary conditions they prescribe when the lubricant film cavitates, and they substantially influence the simulation results.

Sommerfeld first solved the RE for an entire journal bearing, but the solution included regions of negative lubricant film pressure [30]. Gumbel set the non-physical negative pressure results to ambient pressure and only allowed positive pressure values in the solution [31], which became known as the half-Sommerfeld boundary condition because it disregarded the negative half of the full Sommerfeld solution. The HS cavitation model is straightforward to implement in any lubrication simulation. However, its solution does not ensure mass conservation in the cavitation region, leads to a piece-wise continuous pressure solution (due to discontinuous flow rates at the cavitation boundary), and does not accurately identify the location of lubricant film rupture or reformation. Swift [32] and Stieber [33] proposed additional boundary conditions to ensure that the spatial derivative of the lubricant film pressure is zero at the location of film rupture, which became known as the Reynolds boundary condition, but also does not ensure mass conservation or account for lubricant film reformation. Alternatively, Jakobsson and Floberg [34] and Olsson [35] presented the idea of continuity equations to ensure mass conservation in the cavitation region. Elrod and Adams [36] and later Elrod [37] introduced a computer algorithm to implement the JFO boundary condition in numerical simulations. This algorithm involved a switch function to distinguish between solving the lubricant film pressure in a full film region, and a fraction film region with cavitation. Updates to this original algorithm have been implemented by, e.g., Vijayaraghavan and Keith [38], Fesanghary and Khonsari [39], and Miraskari et al. [40], each geared towards increasing computational efficiency and reducing convergence problems. The JFO cavitation model enforces mass conservation in the cavitation region and accurately computes the locations of film rupture and reformation. However, the Elrod implementation of the JFO cavitation model is also more computationally intensive, and more prone to stability and convergence problems than the other cavitation models.

Recently, efficient solutions for the JFO cavitation model that do not rely on the Elrod algorithm have been proposed. Woloszynski et al. introduced an algorithm based on complementarity conditions and a system of Fischer–Burmeister equations, which calculated accurate lubricant film pressure

results for several bearing geometries, and reduced the computation time by two orders of magnitude compared to the Elrod implementation of the JFO cavitation model [41]. Biboulet and Lubrecht used a similar method for mass-conserving cavitation to study textured bearing surfaces with fast convergence [42]. Mezzadri and Galligani implemented an inexact Newton method to solve complementarity problems and showed global convergence for mass-conserving lubrication problems [43]. Giacomini et al. also employed complementarity conditions and formulated a finite element solution method for mass-conserving cavitation problems [44]. These modern approaches are computationally efficient and avoid many of the convergence and stability problems inherent to traditional Elrod algorithms.

Some researchers have also proposed cavitation models for specific lubrication conditions. Coyne and Elrod proposed boundary conditions to describe lubricant separation from one bearing surface by accounting for surface tension, using both NS [45] and RE [46]. Their cavitation model shows good agreement with experimental results of a cylindrical-shaped slider bearing. Furthermore, Song et al. derived a mass-conserving cavitation model for gaseous cavitation [47], which provided similar results to the JFO theory with an appropriate choice of cavitation threshold. However, the gaseous cavitation model is independent of a specific cavitation threshold, whereas the other cavitation models depend on a user-defined cavitation threshold. Hirayama et al. implemented an equivalent flow cavitation model in which the viscosity and density are allowed to change [48]. Their numerical predictions of cavitation aligned with high-speed photography results of a textured rotating shaft lubricated with oil. Bayada and Chupin [49] and Bayada [50] proposed a fully compressible, mass-conserving cavitation model that allows for variation in viscosity and density with changing pressure. Their cavitation model produced lubricant film pressure solutions similar to the JFO cavitation model and also allowed for a small region of sub-ambient lubricant film pressure, which has been observed in several bearing experiments [51], but is not allowed in traditional cavitation models.

Comparisons between cavitation models reveal the operating conditions that require using the computationally intensive mass-conserving cavitation models. Liu et al. [52] determined that lubrication simulations of journal bearings with HS and Reynolds cavitation models led to comparable lubricant film pressure results for the range of operating conditions they evaluated. Ausas et al. compared the results of JFO and Reynolds cavitation models in hydrodynamic lubrication (HL) simulations of textured hard-on-hard bearing surfaces [53]. They found that both cavitation models yield similar results for untextured journal bearings, but in a textured bearing, the Reynolds cavitation model underestimates the size of the cavitation region and overestimates

the lubricant film pressure compared to the JFO cavitation model. Zhang and Meng also compared JFO and Reynolds cavitation boundary conditions in HL simulations of textured hard-on-hard bearing surfaces, and additionally compared their results to RoD experiments [54]. They showed that the JFO cavitation model could accurately predict the size and shape of the cavitation region when using the correct cavitation threshold. They also determined that the Reynolds cavitation model predicted a smaller cavitation region and a thicker lubricant film than experimental observations. Wang et al. compared the JFO, HS, and Reynolds cavitation models in an EHL simulation of surfaces with groove texture features for a range of material stiffness values [55]. They showed that the choice of cavitation threshold affects the lubricant film pressure solution, and that the Reynolds cavitation model underestimates and the HS cavitation model overestimates the size of the cavitation region. Qiu and Khonsari performed HL simulations of hard-on-hard textured surfaces using the three cavitation models, two different sizes of texture features, and three different bearing operating conditions [56]. They concluded that both the HS and Reynolds cavitation models overestimated the lubricant film pressure, whereas the HS cavitation model overestimated and the Reynolds cavitation model underestimated the size of the cavitation region, which is in agreement with results obtained by others (e.g., [55]). They also showed that the different cavitation models yield similar lubricant film pressure results for small texture features (150 μm diameter, 10 μm depth), and that with increasing texture aspect ratio the JFO and Reynolds cavitation models predict increasing and decreasing lubricant film pressure, respectively.

Thus, from the literature, it is well-known that different cavitation models result in different solutions of the RE, driven by their different implementations of the cavitation physics. As evidenced by experimental verification, it is commonly understood that the JFO cavitation model is the most accurate one because it accounts for mass conservation, which the others do not. However, no publications exist in the open literature that systematically evaluate the difference between the results of the RE in the case of soft EHL of textured parallel slider bearings, when considering different cavitation models and a range of texture design parameters and bearing operating conditions. Furthermore, most publications calculate the lubricant film pressure for a constant bearing surface separation (e.g., [55, 56]), rather than calculating the lubricant film thickness for a constant bearing load-carrying capacity. The latter results are useful for designing textured bearing surfaces, because the lubricant film thickness is typically not an input variable but results from the bearing design and operating parameters, for instance, in the context of hard-on-soft prosthetic hip implants. Thus, the objective of this paper is to quantify and compare the lubricant film thickness in a textured

hard-on-soft bearing using soft EHL simulations with different cavitation models, covering the entire useful range of texture design parameters and a wide range of bearing operating conditions relevant to prosthetic hip implants.

2 Methods

2.1 Soft EHL Model

Figure 1 schematically illustrates the soft EHL model of a hard-on-soft textured bearing we consider in this paper. We simulate an array of five spherical texture features on a rigid surface, sliding with velocity U , parallel to a smooth, deformable polyethylene surface. The model represents a small portion in the center of a textured, hard-on-soft prosthetic hip implant bearing and, thus, allows neglecting the curvature and eccentricity of the prosthetic hip implant. The lubricant film thickness $h(x,y)$, is the sum of the nominal bearing surface separation c , the texture feature geometry, and the polyethylene deformation $d(x,y)$. We describe the texture features using the texture aspect ratio $\varepsilon = h_p/2r_p$ and

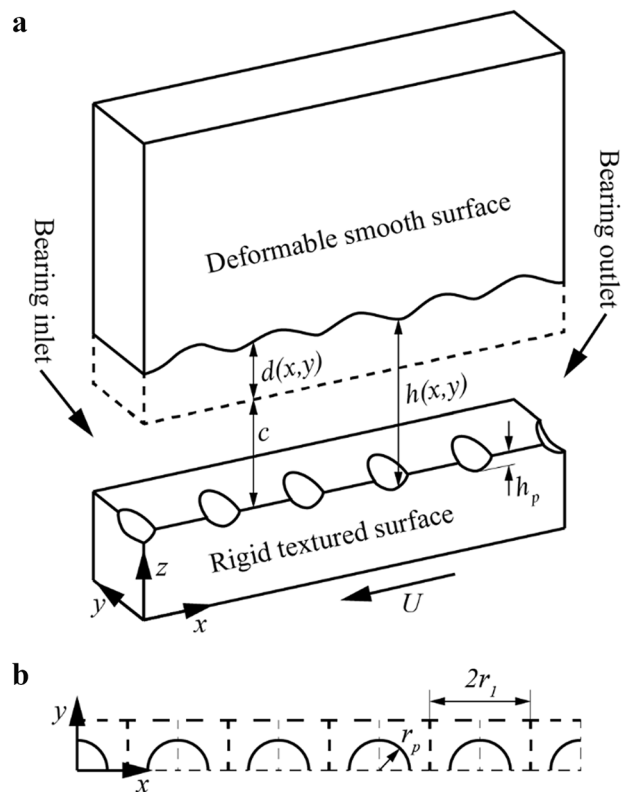


Fig. 1 **a** Schematic of the soft EHL model of a textured hard-on-soft bearing showing the smooth, deformable surface sliding relative to the rigid textured surface. Dashed lines illustrate the undeformed shape of the smooth surface. **b** Top view of the array of five texture features

the texture density $S_p = \pi r_p^2 / 4r_l^2$, where h_p is the depth and r_p is the radius of the texture feature ($r_p = 50 \mu\text{m}$ in this work), and $2r_l$ is the length of a square unit cell that bounds each texture feature. The model shows symmetry at the edges and center of the array of texture features and, thus, we only simulate half of the width of a square unit cell (see Fig. 1). The bearing inlet and outlet occur in the center of a texture feature because mass-conserving cavitation algorithms do not generate positive bearing load-carrying capacity in numerical simulations of fully textured parallel sliding surfaces unless the bearing inlet is textured [57]. We simulate steady-state sliding for computational feasibility and numerical stability, similar to other numerical simulations, e.g., [58]. However, we cover a broad range of steady-state bearing operating conditions to study the effect of sliding velocity and load-carrying capacity on the lubricant film thickness.

We solve the two-dimensional (2D), iso-viscous, isothermal, steady-state RE to calculate the lubricant film pressure, i.e.,

$$\frac{\partial}{\partial x} \left(h^3 \frac{\partial p}{\partial x} \right) + \frac{\partial}{\partial y} \left(h^3 \frac{\partial p}{\partial y} \right) = 6\mu U \frac{\partial h}{\partial x} \quad (1)$$

where x and y are Cartesian coordinates, $p(x,y)$ is the lubricant film pressure, $h(x,y)$ is the lubricant film thickness, μ is the dynamic viscosity of the lubricant, and U is the relative sliding velocity between both bearing surfaces. We non-dimensionalize Eq. (1) to render its solution independent of any particular lubrication system, similar to previous work (see, e.g., [59]). We define $X = x/r_p$, $Y = y/r_p$, $P = p/p_0$, $H = h/c$, where $p_0 = 101,325 \text{ Pa}$ is atmospheric pressure, $\lambda = 3\mu U / 2r_p p_0$ is the flow factor, which incorporates the bearing operating conditions, and $\delta = c/2r_p$ is the non-dimensional bearing surface separation. Thus,

$$\frac{\partial}{\partial X} \left(H^3 \frac{\partial P}{\partial X} \right) + \frac{\partial}{\partial Y} \left(H^3 \frac{\partial P}{\partial Y} \right) = \frac{\lambda}{\delta^2} \frac{\partial H}{\partial X} \quad (2)$$

Figure 2 shows a flow chart of the numerical simulation methodology, which simultaneously solves three equations: the lubricant film pressure (RE), the polyethylene deformation (elasticity equations), and the balance between the bearing load-carrying capacity and an external bearing load. We assume an initial bearing surface separation and calculate the lubricant film pressure [Eq. (2)], while maintaining the bearing inlet ($x=0$) and outlet ($x=10r_l$) at atmospheric pressure. This is a common choice for simulations of textured bearing surfaces, including prosthetic hip implants (see, e.g., [27, 60]), because the lubricant film pressure varies within each texture feature as a result of its diverging and converging geometry and it is equal to the atmospheric pressure near the inlet of each texture feature. However, we also note that the inlet and outlet pressure boundary conditions have

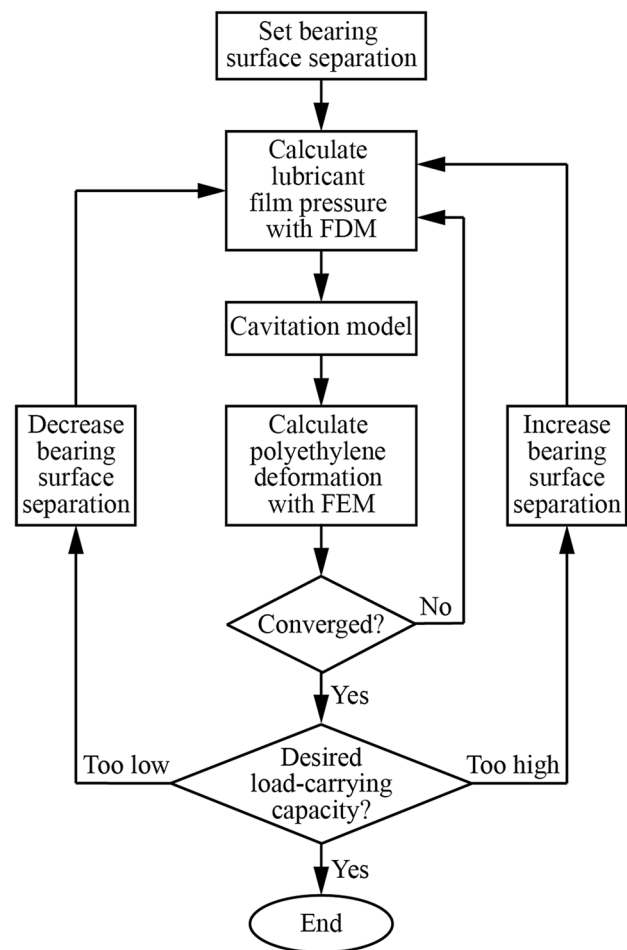


Fig. 2 Flowchart of the soft EHL numerical simulation methodology with different cavitation models

negligible effect on the lubricant film thickness and pressure simulation results. The boundary conditions are chosen to represent a pattern of texture features that continues in the x - and y -directions beyond the small portion we simulate. We apply symmetry boundary conditions at the lateral edge ($y = r_l$) and center ($y = 0$) of the solution domain to simulate the effect of adjacent texture features on the bearing surface, while capitalizing on geometric symmetry for computational efficiency. We iteratively solve Eq. (2) using the finite difference method (FDM) with central discretization on a two-level multi-grid [61] and 301 nodes across each square unit cell, until the L2-norm of the difference between consecutive iterative solutions is less than 0.001 (based on a convergence analysis). Hence, the model comprises a total of $5 \times 301 \times 151 = 227,255$ unknowns.

We use the finite element method (FEM) to calculate the elastic deformation of the polyethylene bearing surface, subject to the solution of the lubricant film pressure calculation. We consider a 3 mm thick piece of UHMWPE with linear elastic constitutive equations ($E = 0.9 \text{ GPa}$ and $\nu = 0.46$

[62]). The maximum lubricant film pressure remains far below the yield stress of UHMWPE ($\sigma_y = 10$ MPa) and, thus, we do not consider plasticity in this model. We constrain the top face of the UHMWPE in all directions and apply symmetry boundary conditions in the lateral directions to the inlet, outlet, and side faces. We apply the lubricant film pressure to the bottom face as a pressure load normal to the surface. Since the polyethylene surface is not free to rotate, the shear forces acting on the polyethylene face have a negligible effect on the lubricant film thickness compared to the pressure. Mesh convergence analysis shows that 20 elements across a square unit cell ($2r_f$) and 40 elements along the polyethylene thickness yield a converged solution. The polyethylene deformation solution updates the lubricant film thickness and necessitates a new calculation of lubricant film pressure. We iterate between solutions of the lubricant film pressure and the polyethylene deformation until the L2-norm of the difference between successive iterations is less than 0.001. We compare the load-carrying capacity of the textured bearing $W = \iint P(X, Y) dXdY = P_{\text{avg}}$ to the external bearing load, and change the non-dimensional bearing surface separation δ until the bearing load-carrying capacity, polyethylene deformation, and lubricant film pressure converge simultaneously.

We compare the lubricant film thickness of soft EHL simulations of the textured hard-on-soft bearing (Fig. 1) with different cavitation models, and consider a broad range of bearing operating conditions (bearing load-carrying capacity and flow factor) and texture design parameters (texture aspect ratio and texture density). Table 1 identifies the parameters we consider, showing their nominal value and corresponding range, selected to be relevant to prosthetic hip implants. However, the range of flow factors covers an order of magnitude to accommodate different lubricants and sliding velocities and ensure full film lubrication. Thus, it exceeds the range typically relevant to prosthetic hip implants for the size of texture features considered here ($r_p = 50$ μm). To obtain flow factors with realistic values of viscosity and sliding velocity, one could reduce the size of the texture features. Note that the assumption of an artificially high lubricant viscosity is a commonly accepted approximation for similar simulations (see, e.g., [63]). We evaluate three external bearing loads: 0.250, 0.500, and 0.750 MPa, which correspond to bearing load-carrying capacities of 2.467, 4.935, and 7.402, and are relevant to

replicate wear mechanisms and wear rates observed clinically in UHMWPE acetabular liners [64].

We determine the minimum lubricant film thickness for each combination of bearing operating conditions and texture design parameters, because it is representative of where solid-on-solid contact between the bearing surfaces may first occur. Furthermore, we determine the optimum texture design parameters that maximize the minimum lubricant film thickness. To use consistent terminology, we refer to it as the “optimum” lubricant film thickness, i.e., the lubricant film thickness that corresponds to the optimum texture design parameters. We consider $0.2 \leq S_p \leq 0.7$, noting that the theoretical maximum value $S_{p,\text{max}} = \pi/4$, and $0.020 \leq \varepsilon \leq 0.100$ based on previous results, e.g., [26, 28]. We extend the range of ε if needed to find the optimum texture design parameters.

2.2 Cavitation Models

Cavitation has been demonstrated experimentally in textured bearing surfaces at flow factors similar to realistic conditions, see, e.g., [54], but we are unaware of any experimental work that has quantified the cavitation threshold in joint fluid. However, gaseous cavitation occurs in the textured bearing at a cavitation threshold between atmospheric pressure and the vapor pressure of the lubricant. We consider the HS, Reynolds, and JFO cavitation models, and enforce a cavitation threshold equal to the vapor pressure of water (5630 Pa), which is a conservative worst-case scenario compared to simulations that use a cavitation threshold equal to atmospheric pressure (see, e.g., [27]). We note that the vapor pressure of water is close to the reported vapor pressure of blood plasma [65], which is the major component of joint fluid. The HS cavitation model enforces the cavitation threshold after calculating the lubricant film pressure, and effectively resets any pressure below the cavitation threshold to that threshold. In contrast, the Reynolds cavitation model enforces the cavitation threshold on every iteration of the numerical solution to ensure that the spatial derivative of the lubricant film pressure is zero at the location of film rupture. Finally, the Elrod implementation of the JFO cavitation model requires modifying the RE. Following the process outlined by Wang et al. [55], we introduce a fractional film content parameter, $0 \leq \theta \leq 1$, to the right-hand side of Eq. (2), i.e.,

Table 1 Bearing operating conditions and texture design parameters, showing nominal, minimum, and maximum value

Parameter	Nominal value	Minimum value	Maximum value
Flow factor, λ	0.300	0.060	0.300
Bearing load-carrying capacity, W	4.935	2.467	7.402
Texture density, S_p	0.200	0.200	0.700
Texture aspect ratio, ε	0.020	0.020	0.100

$$\frac{\partial}{\partial X} \left(H^3 \frac{\partial P}{\partial X} \right) + \frac{\partial}{\partial Y} \left(H^3 \frac{\partial P}{\partial Y} \right) = \frac{\lambda}{\delta^2} \frac{\partial}{\partial X} (\theta H) \tag{3}$$

We consider two regimes [full film and fractional film (cavitation)], similar to the algorithm by Elrod and Adams [37]. In the full film regime, $\theta = 1$, and Eq. (3) reduces to the non-dimensional RE (Eq. (2)). In the fractional film regime, the lubricant film pressure is the cavitation threshold $P = P_{cav}$, and we solve Eq. (3) for the fractional film content, $\theta(X, Y)$. Each point in the full film regime can switch to the fractional film regime if the lubricant film pressure decreases to the cavitation threshold. Likewise, each point in the cavitation regime can switch to the full film regime if the fractional film content increases to unity. Using this method, we have successfully recreated the published results of other textured bearings, e.g., [39, 55].

Table 2 illustrates the implementation of each cavitation model with pseudo code.

3 Results and Discussion

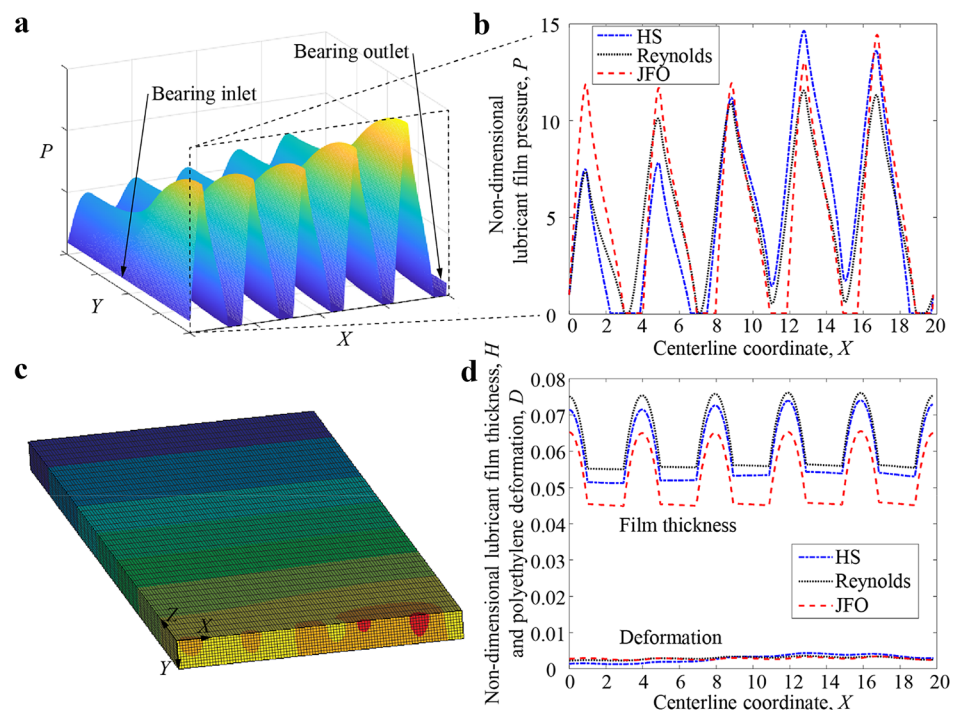
3.1 Typical Soft EHL Solutions

Figure 3 illustrates a typical result of a soft EHL simulation of a textured hard-on-soft bearing with $\lambda = 0.300$, $W = 4.935$, $\epsilon = 0.020$, and $S_p = 0.200$. Figure 3a shows a three-dimensional (3D) view of the lubricant film pressure across the array of texture features (solution domain), whereas Fig. 3b depicts the lubricant film pressure along the centerline of the texture features, showing results for the three cavitation models (note that the bearing inlet is on the left). Figure 3c shows the polyethylene deformation superimposed on the

Table 2 Pseudo code for the three cavitation models

Cavitation model	HS	Reynolds	JFO
Pseudo code	While not converged For all i, j Solve Eq. (2) for $P(i, j)$ End for End while For all i, j If $P(i, j) < P_{cav}$ $P(i, j) = P_{cav}$ End if End for	While not converged For all i, j Solve Eq. (2) for $P(i, j)$ If $P(i, j) < P_{cav}$ $P(i, j) = P_{cav}$ End if End for End while	While not converged For all i, j If full film regime $\theta(i, j) = 1$ Solve Eq. (3) for $P(i, j)$ Else if cavitation regime $P(i, j) = P_{cav}$ Solve Eq. (3) for $\theta(i, j)$ End if End for End while

Fig. 3 Typical soft EHL simulation results for a textured hard-on-soft bearing with $\lambda = 0.300$, $W = 4.935$, $\epsilon = 0.020$, and $S_p = 0.200$. **a** 3D view of the non-dimensional lubricant film pressure across the solution domain. **b** Non-dimensional lubricant film pressure along the centerline of the texture features. **c** Polyethylene deformation superimposed on the FEM mesh. **d** Non-dimensional polyethylene deformation and lubricant film thickness along the centerline of the texture features



FEM mesh and Fig. 3d depicts the polyethylene deformation and lubricant film thickness along the centerline of the texture features, showing results for the three cavitation models. We present the lubricant film thickness normalized with the texture feature diameter, i.e., $H = h/2r_p$, rather than normalized with the nominal bearing surface separation, $H = h/c$, as used for the simulations. This allows comparing the results from simulations with different bearing surface separation values c .

We observe from Fig. 3 that the soft EHL simulations with different cavitation models result in different lubricant film pressure and thickness, despite identical bearing load-carrying capacity. The bearing load-carrying capacity is the integral of the lubricant film pressure across the entire bearing surface and, thus, the results for the three different cavitation models show the same area under their respective lubricant film pressure curve. The lubricant film pressure increases where the bearing surfaces converge and reaches a local maximum at the outlet of the texture feature where the bearing surfaces are parallel, before decreasing to the cavitation threshold by the inlet of the adjacent downstream texture feature, where the bearing surfaces diverge. Note that the JFO and Reynolds cavitation models predict film rupture at the same locations, whereas the HS cavitation model predicts film rupture farther upstream. This is because the JFO and Reynolds cavitation models enforce pressure continuity at the point of film rupture and the HS cavitation model does not. The Reynolds cavitation model immediately reforms the lubricant film and increases the lubricant film pressure after film rupture, whereas the other cavitation models predict a larger cavitation region before film reformation. The mass-conserving JFO cavitation model predicts similar-sized cavitation regions at the inlet of each texture feature in the bearing, whereas the HS cavitation model allows different sized cavitation regions in each texture feature of the bearing and does not predict cavitation in the last two full texture features of the bearing. The simulation with the JFO cavitation model predicts a thinner lubricant film than the other cavitation models because not enforcing mass conservation allows more lubricant to exist between the bearing surfaces to generate bearing load-carrying capacity. We also observe that the simulation with the JFO cavitation model reaches a higher maximum lubricant film pressure and shows a steeper gradient than the results with the Reynolds cavitation model, because both models have the same bearing load-carrying capacity, but the JFO cavitation model reaches the maximum pressure in a shorter distance (along the X -coordinate) as a result of the larger cavitation region compared to the Reynolds cavitation model.

We quantify the fraction of the texture features that experiences cavitation for simulations with the Reynolds and JFO cavitation models, respectively. The size of the cavitation regions in each texture feature varies when using the HS

cavitation model, whereas it remains almost constant when using the Reynolds and JFO cavitation models. Figure 4a shows a contour plot with lines of constant non-dimensional lubricant film pressure P around the first full texture feature in the bearing using the Reynolds cavitation model, and Fig. 4b shows the same contour plot using the JFO cavitation model. The dashed line shows the circular outline of the texture feature on the rigid bearing surface. We illustrate the size of the cavitation region as a gray-shaded area.

From Fig. 4, we observe that cavitation occurs just inside the inlet of the texture features for the Reynolds cavitation model, whereas the cavitation region extends into the front half of the texture features for the JFO cavitation model. We calculate the cavitation area ratio as the area of the cavitation region on the bearing surface divided by the total area of the texture features on the bearing surface and calculate 0.046 and 0.383 for the Reynolds and JFO cavitation models, respectively. This cavitation area ratio remains approximately constant for all simulations, independent of the texture design parameters and bearing operating conditions. We point out that Zhang and Meng used HL simulations and RoD experiments in tandem with high-speed photography to demonstrate that the cavitation area ratio of hard-on-hard bearings with groove texture features increases asymptotically with increasing bearing sliding velocity,

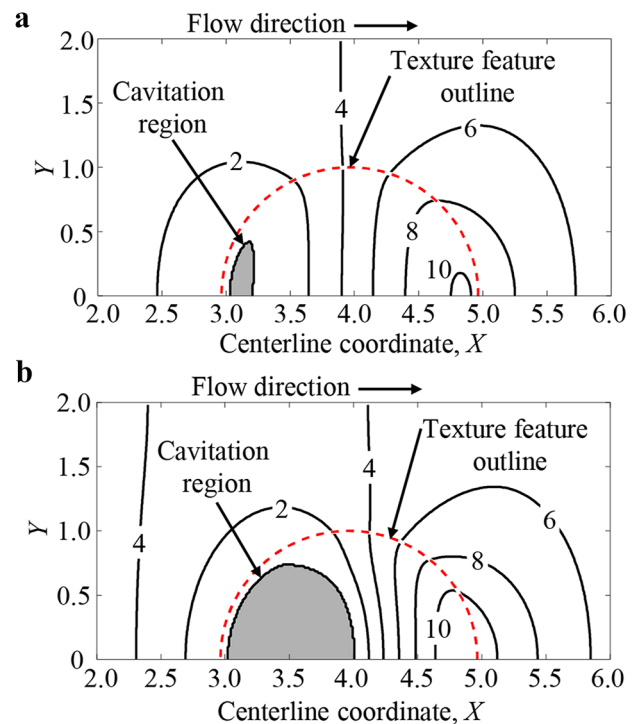


Fig. 4 Contour lines of constant non-dimensional lubricant film pressure $P = p/p_0$ across a single texture feature (red dashed line) on the bearing surface, using **a** Reynolds, and **b** JFO cavitation models, identifying the cavitation region (gray) (color figure online)

and demonstrated the same result experimentally for circular texture features [54]. Thus, for constant texture feature geometry and bearing load-carrying capacity, we expect the size of the cavitation region to increase with increasing flow factor because a faster (or more viscous) lubricant flow leads to more variation in the lubricant film pressure (higher maximum and lower minimum pressure). However, the cavitation threshold limits the minimum lubricant film pressure and, thus, the size of the cavitation region increases. The size of the cavitation region asymptotically approaches a constant value with increasing flow factor because of backflow and choking of the lubricant flow, which also prevent the lubricant film thickness from increasing indefinitely. We calculate the flow factor for Zhang and Meng's experiments to be two orders of magnitude smaller than the flow factors considered in our work, thus indicating that the range of bearing operating conditions evaluated in this paper correspond to the maximum cavitation area ratio, which then can be expected to remain almost constant.

We also compare our soft EHL simulations to HL simulations between two rigid surfaces. Figure 5 shows contour plots with lines of constant non-dimensional lubricant film pressure across the entire bearing surface for the nominal texture design parameters and bearing operating conditions ($\lambda = 0.300$, $W = 4.935$, $\varepsilon = 0.020$, $S_p = 0.200$),

and showing (a) HL and (b) EHL with the HS cavitation model, (c) HL and (d) EHL with the Reynolds cavitation model, and (e) HL and (f) EHL with the JFO cavitation model. We illustrate the outline of the spherical texture features with red dashed lines, and the cavitation regions with gray-shaded areas. Note that for clarity, we do not label contour lines of non-dimensional lubricant film pressure greater than $P = 11$ because the contour lines are too close together.

From Fig. 5, we observe that the surface deformation in the EHL simulations affects the lubricant film pressure and the size of the cavitation region compared to the HL simulations with rigid bearing surfaces. We observe from the HL simulation results (Fig. 5a, c, e) that the size of the cavitation region remains almost constant in each texture feature, and that the maximum lubricant film pressure is higher than in the EHL simulations (Fig. 5b, d, f), where the size of the cavitation region decreases in downstream texture features. This is because the EHL simulations experience the greatest deformation in the last two full texture features on the bearing surface (see Fig. 3d), which increases the volume of lubricant between the bearing surfaces and decreases the cavitation region within those texture features. Table 3 shows the cavitation area ratio, averaged over all texture features in the bearing, for HL and EHL simulations and with the three cavitation models.

Fig. 5 Contour lines of constant non-dimensional lubricant film pressure P across the textured bearing surface. **a** HL and **b** EHL with the HS cavitation model, **c** HL and **d** EHL with the Reynolds cavitation model, and **e** HL and **f** EHL with the JFO cavitation model

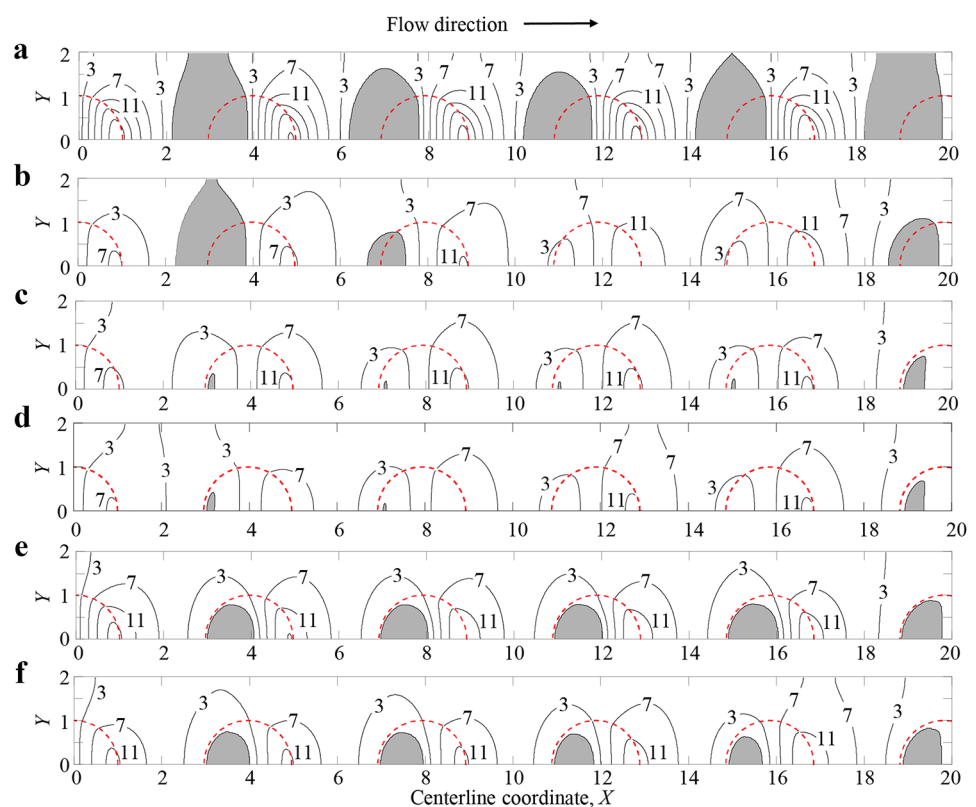


Table 3 Cavitation area ratios for HL/EHL simulations with different cavitation models

Cavitation model	HL simulation	EHL simulation
HS	1.606	0.508
Reynolds	0.047	0.047
JFO	0.444	0.336

3.2 Effect of Texture Feature Location and Cavitation Threshold

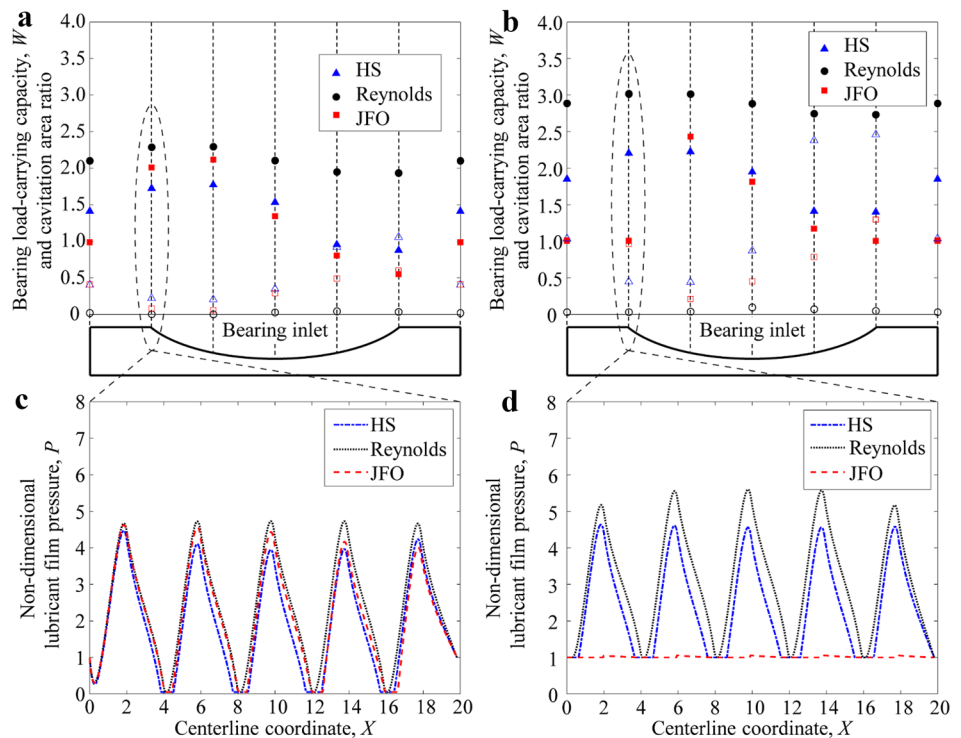
We perform simulations with the bearing inlet at different locations with respect to the first texture feature and with different values of the cavitation threshold to understand their effect on the lubricant film thickness. We use the nominal texture design parameters and bearing operating conditions, i.e., $S_p = 0.200$, $\epsilon = 0.020$, $\lambda = 0.300$, and we specify a non-dimensional bearing surface separation $\delta = 0.075$ and calculate the resulting bearing load-carrying capacity W . Figure 6a shows the bearing load-carrying capacity as a function of the bearing inlet location with solid markers, and the cavitation area ratio as a function of the bearing inlet location with open markers for $p_{cav} = 5,630$ Pa. Figure 6b shows the same results for simulations with a cavitation threshold $p_{cav} = 101,325$ Pa. We also show a cross-section of a texture feature to illustrate the location of the bearing inlet at each location we evaluate, and we match the inlet locations with the corresponding results using vertical dashed

lines. Figure 6c depicts the lubricant film pressure along the centerline of the textured bearing, showing results for the three cavitation models, and the texture feature inlet coincides with the bearing inlet and $p_{cav} = 5630$ Pa. Figure 6d shows the same lubricant film pressure along the centerline of the textured bearing and $p_{cav} = 101,325$ Pa.

From Fig. 6a, we observe that the Reynolds cavitation model predicts the greatest bearing load-carrying capacity and the smallest cavitation region. The load-carrying capacity simulated with the Reynolds cavitation model also exhibits the least variation in terms of the location of the texture feature inlet with respect to the bearing inlet, compared to the other two cavitation models. Additionally, we observe that the cavitation area ratio inversely relates to the bearing load-carrying capacity.

Comparing Fig. 6a and b, we observe that increasing the cavitation threshold slightly increases the bearing load-carrying capacity because the lubricant film pressure cannot decrease below $p_{cav} = 101,325$ Pa. When the bearing inlet coincides with the parallel region between texture features, the JFO cavitation model predicts no bearing load-carrying capacity ($W = 1$) because the cavitation area ratio is approximately equal to 1, i.e., cavitation fills the entire texture feature. This is similar to results documented by Dobrica and Fillon for fully textured parallel sliding bearings [57]. Additionally, we observe that the bearing load-carrying capacity decreases by 49.8% when the texture feature inlet coincides with the bearing inlet, for the JFO cavitation model with $p_{cav} = 101,325$ Pa compared to $p_{cav} = 5630$ Pa, because the

Fig. 6 Bearing load-carrying capacity (solid markers) and cavitation area ratio (open markers) as a function of the bearing inlet location for **a** $p_{cav} = 5630$ Pa, and **b** $p_{cav} = 101,325$ Pa. Non-dimensional lubricant film pressure along the centerline coordinate, when the texture feature inlet coincides with the bearing inlet and **c** $p_{cav} = 5630$ Pa and **d** $p_{cav} = 101,325$ Pa



high cavitation threshold causes cavitation in the texture features that does not occur with the low cavitation threshold. Figure 6c illustrates the situation where the bearing inlet and the texture feature inlet coincide and $p_{cav} = 5630$ Pa. We observe that the lubricant film pressure decreases within the diverging channel at the bearing inlet but does not reach the cavitation threshold. Since no cavitation occurs in the first texture feature, all the lubricant in the first texture feature flows downstream to the other texture features in the bearing. Figure 6d illustrates the same situation as Fig. 6c but with $p_{cav} = 101,325$, and cavitation occurs in the first texture feature. The mass-conserving JFO cavitation model limits the volume of lubricant that flows to the remainder of the bearing because of cavitation in the first texture feature.

The effect of the location of texture features with respect to the bearing inlet is important for numerical simulations, but less so for physical experiments because numerical simulations can exactly define the geometry and boundary conditions to study these effects (see, e.g., [66]). In contrast, experiments with textured surfaces show an increase of bearing load-carrying capacity and decrease of friction and wear compared to smooth surfaces, even when the texture features are not explicitly placed at the bearing inlet (see, e.g., [20, 67]). In many experimental configurations, including a ball-in-socket prosthetic hip implant, the bearing inlet cannot be precisely defined with respect to the texture features, or the bearing inlet location changes during the experiments. In these instances, the changing texture feature location with respect to the bearing inlet may result in

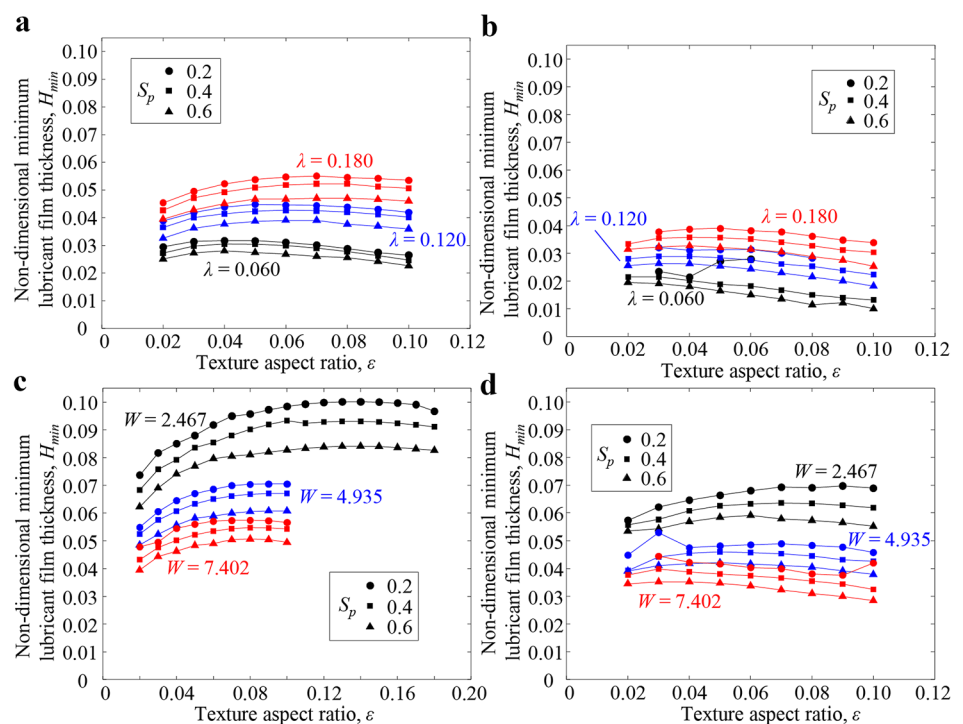
a “net” bearing load-carrying capacity as the bearing cycles through the different texture feature locations with respect to the bearing inlet.

3.3 Effect of Bearing Operating Conditions

In the remainder of this paper, we compare the Reynolds and JFO cavitation models without the HS cavitation model because the latter is known to be inaccurate, e.g., [47]. Figure 7a and b show the minimum non-dimensional lubricant film thickness H_{min} as a function of the texture aspect ratio ϵ , for different values of the texture density S_p and flow factor λ , with a constant bearing load-carrying capacity $W = 4.935$, calculated with (a) the Reynolds cavitation model and (b) the JFO cavitation model, respectively. Figure 7c and d show H_{min} as a function of the texture aspect ratio ϵ , with a constant flow factor $\lambda = 0.300$, and different values of the bearing load-carrying capacity W , calculated with (c) the Reynolds cavitation model and (d) the JFO cavitation model, respectively.

From Fig. 7a, we observe that the minimum lubricant film thickness increases with increasing flow factor because increasing the flow factor also increases the lubricant viscosity and/or the relative sliding velocity between the bearing surfaces. We observe that an optimum texture aspect ratio exists that maximizes the minimum lubricant film thickness for each bearing operating condition. Comparing Fig. 7a and b, we observe that the Reynolds cavitation model predicts a thicker lubricant film than the JFO cavitation model,

Fig. 7 Minimum non-dimensional lubricant film thickness as a function of texture aspect ratio with $W = 4.935$ and various flow factor λ for **a** Reynolds cavitation model, and **b** JFO cavitation model. Minimum non-dimensional lubricant film thickness with $\lambda = 0.300$ and various bearing load-carrying capacity W for **c** Reynolds cavitation model, and **d** JFO cavitation model



because failing to conserve mass in the cavitation region allows more lubricant to flow between the bearing surfaces. We also observe that the Reynolds cavitation model predicts a greater optimum texture aspect ratio than the JFO cavitation model for each of the different bearing operating conditions, because the Reynolds cavitation model enforces conservation of the mass flow rate at the film rupture boundary, but not at film reformation boundary. Increasing the texture aspect ratio increases the texture feature volume, potentially increasing the discrepancy between the mass flow rates into and out of the texture features with cavitation. This appears to contrast the work by Qiu and Khonsari, who showed that the bearing load-carrying capacity increases with increasing texture aspect ratio when using the JFO cavitation model and decreases with increasing texture aspect ratio when using the Reynolds cavitation model [56]. We note that Qiu and Khonsari calculated the bearing load-carrying capacity for a given bearing surface separation, whereas we calculate the lubricant film thickness for a given bearing load-carrying capacity. Thus, the texture aspect ratio that predicts the maximum bearing load-carrying capacity for a given bearing surface separation may not be the same texture aspect ratio that maximizes the lubricant film thickness for a given bearing load-carrying capacity.

From Fig. 7c, we observe that the lubricant film thickness decreases with increasing bearing load-carrying capacity, as expected [26, 68]. Comparing Fig. 7c and d, we note that the Reynolds cavitation model predicts a thicker lubricant film and larger optimum texture aspect ratio than the JFO cavitation model.

We also calculate the optimum texture aspect ratio that maximizes the lubricant film thickness by determining a 3rd order polynomial best-fit (based on least-squares regression) for the data of Fig. 7. Figure 8a shows the optimum texture aspect ratio as a function of the flow factor, and Fig. 8b shows the optimum texture aspect ratio as a function of the bearing load-carrying capacity for both the Reynolds and JFO cavitation models. Figure 8c shows the optimum texture aspect ratio as a function of the optimum lubricant film thickness for both the Reynolds and JFO cavitation models. The dotted line marks a linear best-fit equation for the data from both cavitation models.

From Fig. 8a and b, we observe that the optimum texture aspect ratio increases with increasing flow factor and decreases with increasing bearing load-carrying capacity for both cavitation models. This is because the optimum texture aspect ratio depends on the lubricant film thickness, which is a function of the bearing operating conditions, as we have shown previously [26]. The lubricant film thickness is not explicitly selected by the bearing designer but results from the bearing design parameters and operating conditions. From Fig. 8c, we observe that a proportional relationship exists between the optimum texture aspect ratio and the

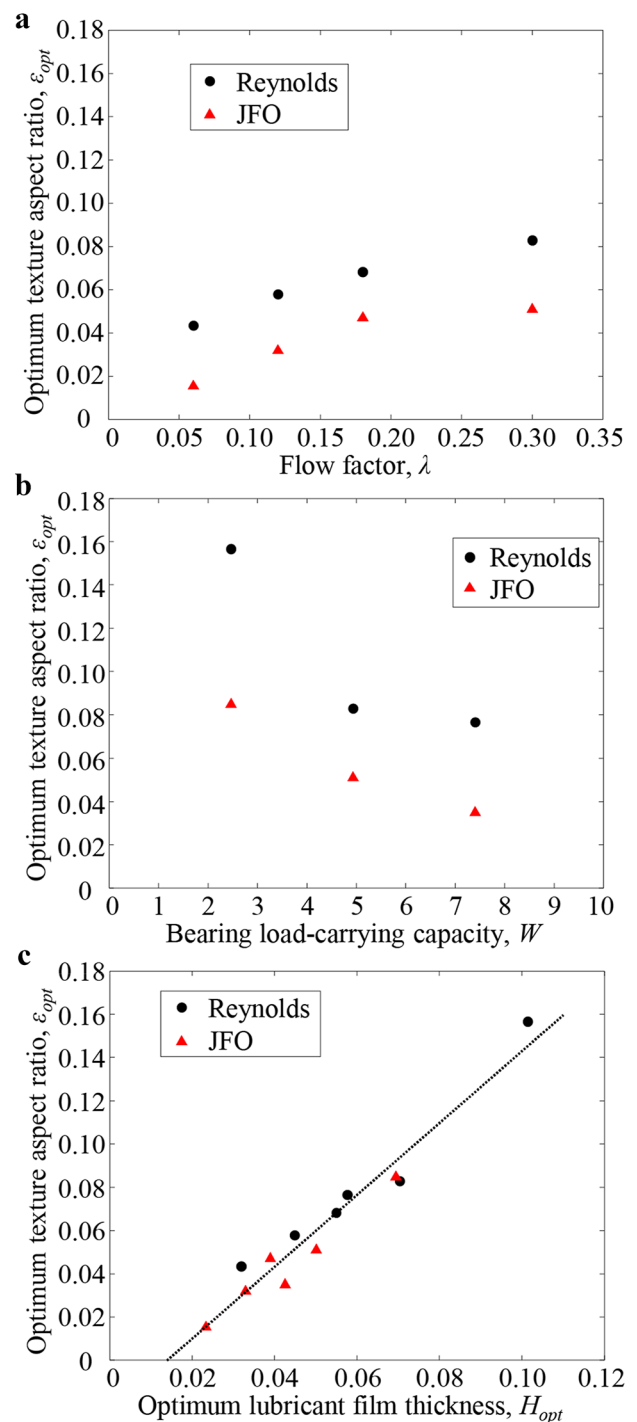


Fig. 8 Optimum texture aspect ratio for the Reynolds and JFO cavitation models **a** as a function of flow factor, **b** as a function of the bearing load-carrying capacity, and **c** as a function of the optimum lubricant film thickness

optimum lubricant film thickness for both cavitation models. We find a linear best-fit equation $\epsilon_{opt} = 1.661H_{opt} - 0.023$, with $R^2 = 0.944$ for both cavitation models. This indicates that the Reynolds cavitation model predicts larger optimum

texture aspect ratios than the JFO cavitation model at each bearing operating condition because it predicts a thicker lubricant film. Furthermore, both cavitation models capture the same proportional change of the optimum texture aspect ratio that accompanies a change in lubricant film thickness, which was also documented by others, e.g., [69].

We note that $S_p = 0.2$ led to the optimum lubricant film thickness in our simulations because we did not evaluate smaller values and, thus, may not have identified the true optimum texture density that maximizes the lubricant film thickness. However, simulations with $S_p < 0.2$ led to instability and/or did not converge with the JFO cavitation model.

3.4 Comparison Between Soft EHL Simulations with Different Cavitation Models

We quantify the percent difference between the lubricant film thickness with the Reynolds and JFO cavitation models as a function of texture design parameters and bearing operating conditions. Figure 9a shows contours of constant percent difference (expressed as a fraction) between the lubricant film thickness calculated with the Reynolds and JFO cavitation models as a function of texture design parameters and bearing operating conditions with constant bearing load-carrying capacity $W = 4.935$. We superimpose three datasets with different flow factors in different colors ($\lambda = 0.06$ (black dotted line), $\lambda = 0.12$ (blue solid line), $\lambda = 0.18$ (red dashed line)). Figure 9b shows contours of constant percent difference (expressed as a fraction) between the lubricant film thickness calculated with the Reynolds and JFO cavitation models as a function of texture design parameters and bearing operating conditions with constant flow factor $\lambda = 0.30$. We superimpose three datasets with different bearing load-carrying capacity in different colors ($W = 2.467$ (black dotted line), $W = 4.935$ (blue solid line), $W = 7.402$ (red dashed line)).

From Fig. 9a, we observe that the percent difference between the JFO and Reynolds cavitation models increases with increasing texture aspect ratio and with increasing texture density. This is because the texture feature volume increases with increasing texture aspect ratio. The JFO cavitation model strictly conserves the mass flow rate in and out of the cavitation region, whereas these mass flow rates can differ with the Reynolds cavitation model, and this discrepancy increases with increasing texture feature volume. We also observe that the percent difference between the cavitation models decreases with increasing flow factor. We observe similar trends in Fig. 9b, when we maintain a constant flow factor and change the bearing load-carrying capacity.

Experiments have documented that the JFO cavitation model is more accurate than the Reynolds cavitation model in terms of calculating the size of the cavitation region and

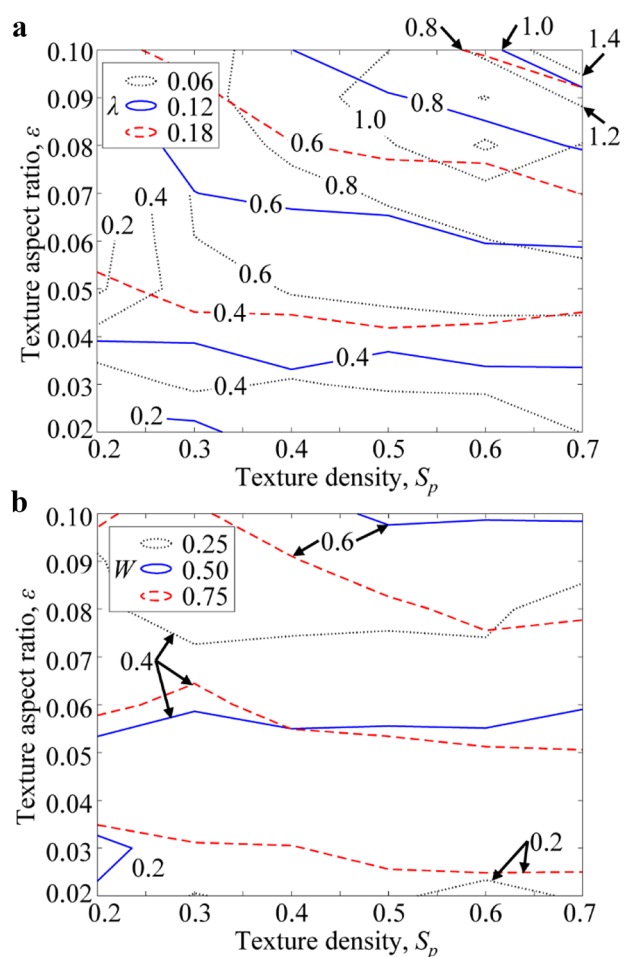


Fig. 9 Contour lines of constant percent difference (expressed as a fraction) between the Reynolds and JFO cavitation models. **a** $W = 4.935$ and various flow factors. **b** $\lambda = 0.30$ and various bearing load-carrying capacities (color figure online)

predicting the lubricant film thickness (see, e.g., [54]). The JFO cavitation model should therefore be used whenever accuracy is the most important consideration. Efficient algorithms for the JFO boundary conditions exist and could be used whenever possible and compatible with for instance existing computer codes (see, e.g., [41]). However, traditional JFO cavitation models based on the Elrod implementation are computationally expensive and prone to instability and convergence problems (see, e.g., [39]). Table 4 lists the arithmetic mean and standard deviation of the runtime and the number of function calls required to obtain a converged solution for the Reynolds and JFO cavitation models used in this work.

The Reynolds cavitation model is best employed for small values of the texture aspect ratio and texture density, and for large values of the flow factor because texture feature designs that approach a flat surface (small texture aspect ratio, small texture density) result in a small difference between both the

Table 4 The mean and standard deviation of the runtime and number of function calls for the Reynolds and JFO cavitation models

Cavitation model	Mean runtime (h)	Standard deviation of runtime (h)	Mean function calls	Standard deviation of function calls
Reynolds	0.596	0.613	12.010	4.378
JFO	7.788	13.460	29.135	52.606

cavitation models. However, it becomes increasingly more important to use a mass-conserving cavitation model with increasing texture aspect ratio and decreasing flow factor. Additionally, for the purpose of revealing trends in the optimum texture design parameters and optimum lubricant film thicknesses, the Reynolds cavitation model is acceptable, when keeping in mind that it predicts larger optimum texture aspect ratios than the JFO cavitation model. If exact values of the optimum texture design parameters and lubricant film thickness are desired, a mass-conserving cavitation model should be used.

3.5 Accuracy and Limitations

The soft EHL model used in this work makes several assumptions. Specifically, the fully flooded, thin film, steady-state, isothermal, and iso-viscous assumptions necessary for Reynolds equation all apply to our model. We also use values of the flow factor that are high enough to ensure full film lubrication without solid-on-solid contact at the specified bearing load-carrying capacity values. Hard-on-soft prosthetic hip implants operate in the mixed lubrication regime under typical operating conditions, for a large portion of the gait cycle [70]. Maximizing the lubricant film thickness could reduce the fraction of the gait cycle during which mixed lubrication occurs and, thus, reduce contact and, consequently, polyethylene wear.

Our results are useful for the range of steady-state bearing operating conditions we have evaluated and under the conditions where the Reynolds equation is valid, and these results can help inform the design of texture features for prosthetic hip implants. However, care should be taken when comparing to a dynamically operating prosthetic hip implant because of the simplifications of the model. Thus, the optimum texture design parameters may differ in dynamic hip joint simulator experiments. In the context of prosthetic hip implants, accounting for shear-thinning lubricants [71], protein film formation [72], or solid-on-solid contact [73] could improve the accuracy of the numerical model. Protein film formation and deposition of wear debris might change the texture geometry slightly over time. However, we expect this to only have a small effect on the lubricant film thickness and pressure, because

protein structures are small compared to the size of texture features considered here [74], the optimum lubricant film thickness is robust with respect to the texture aspect ratio, and our group has previously shown that surface roughness and geometric irregularities inside texture features have negligible effect on the bearing load-carrying capacity and volume flow rate [75].

4 Conclusions

We conclude that:

- (1) The Reynolds cavitation model predicts thicker lubricant films and larger optimum texture aspect ratios than the JFO cavitation model in soft EHL simulations of textured hard-on-soft bearings because of the lack of mass conservation in the Reynolds cavitation model. Including deformation in the soft EHL simulations affects the maximum lubricant film pressure and the size of the cavitation regions.
- (2) The Reynolds and JFO cavitation models both predict the same proportional relationship between the optimum texture aspect ratio and the optimum lubricant film thickness.
- (3) The percent difference between the lubricant film thickness in the soft EHL simulations of textured hard-on-soft bearings computed with the JFO and Reynolds cavitation models increases with increasing texture aspect ratio because the texture feature volume increases with increasing texture aspect ratio, independent of bearing operating conditions. The discrepancy between the mass-conserving JFO cavitation model and the Reynolds cavitation model where the mass flow rates can differ increases with increasing texture feature volume.

Acknowledgements This work was partially supported by the National Institutes of Health, National Institute of Arthritis and Musculoskeletal and Skin Diseases under grant 1R03AR066826-01A1.

Funding This work was partially supported by the National Institutes of Health, National Institute of Arthritis and Musculoskeletal and Skin Diseases under Grant 1R03AR066826-01A1.

Data Availability Source data available by request.

Code Availability We used custom code developed by our lab, in combination with Ansys.

Declarations

Conflict of interest The authors declare no conflicts of interest or competing interests.

References

- Learmonth, I.D., Young, C., Rorabeck, C.: The operation of the century: total hip replacement. *Lancet* **370**, 1508–1519 (2007). [https://doi.org/10.1016/S0140-6736\(07\)60457-7](https://doi.org/10.1016/S0140-6736(07)60457-7)
- Sloan, M., Premkumar, A., Sheth, N.P.: Projected volume of primary total joint arthroplasty in the U.S., 2014 to 2030. *J. Bone Jt. Surg.* **100**, 1455–1460 (2018). <https://doi.org/10.2106/JBJS.17.01617>
- Halawi, M.J., Brigati, D., Messner, W., Brooks, P.J.: Total hip arthroplasty in patients 55 years or younger: Risk factors for poor midterm outcomes. *J. Clin. Orthop. Trauma* **9**, 103–106 (2018). <https://doi.org/10.1016/j.jcot.2016.12.009>
- Foran, J.R.H.: Total hip replacement. <https://orthoinfo.aaos.org/en/treatment/total-hip-replacement>. Accessed 20 Aug 2021
- Heckmann, N.D., Sivasundaram, L., Stefl, M.D., Kang, H.P., Basler, E.T., Lieberman, J.R.: Total hip arthroplasty bearing surface trends in the United States from 2007 to 2014: the rise of ceramic on polyethylene. *J. Arthroplasty* **33**, 1757–1763 (2018)
- Rieker, C., Konrad, R., Schon, R.: In vitro comparison of the two hard-hard articulations for total hip replacements. *Proc. Inst. Mech. Eng. H* **215**, 153–160 (2001)
- Bosker, B.H., Eetema, H.B., Boomsma, M.F., Kollen, B.J., Maas, M., Verheyen, C.C.P.M.: High incidence of pseudotumour formation after large-diameter metal-on-metal total hip replacement. *J. Bone Joint. Surg. Br.* **94-B**, 755–761 (2012). <https://doi.org/10.1302/0301-620x.94b6.28373>
- Choi, I.Y., Kim, Y.S., Hwang, K.T., Kim, Y.H.: Incidence and factors associated with squeaking in alumina-on-alumina THA. *Clin. Orthop. Relat. Res.* **468**, 3234–3239 (2010). <https://doi.org/10.1007/s11999-010-1394-5>
- Evans, J.T., Evans, J.P., Walker, R.W., Blom, A.W., Whitehouse, M.R., Sayers, A.: How long does a hip replacement last? A systematic review and meta-analysis of case series and national registry reports with more than 15 years of follow-up. *Lancet* **393**, 647–654 (2019). [https://doi.org/10.1016/S0140-6736\(18\)31665-9](https://doi.org/10.1016/S0140-6736(18)31665-9)
- Rajaei, S.S., Campbell, J.C., Mirocha, J., Paiement, G.D.: Increasing burden of total hip arthroplasty revisions in patients between 45 and 64 years of age. *J. Bone Jt. Surg.* **100**, 449–458 (2018)
- Harris, W.H.: Wear and periprosthetic osteolysis: the problem. *Clin. Orthop. Relat. Res.* **393**, 66–70 (2001)
- Liu, A., Richards, L., Bladen, C.L., Ingham, E., Fisher, J., Tipper, J.L.: The biological response to nanometre-sized polymer particles. *Acta Biomater.* **23**, 38–51 (2015). <https://doi.org/10.1016/j.actbio.2015.05.016>
- Capello, W.N., D'Antonio, J.A., Ramakrishnan, R., Naughton, M.: Continued improved wear with an annealed highly cross-linked polyethylene. *Clin. Orthop. Relat. Res.* **469**, 825–830 (2011). <https://doi.org/10.1007/s11999-010-1556-5>
- Laurent, M.P., Johnson, T.S., Crowninshield, R.D., Blanchard, C.R., Bhambri, S.K., Yao, J.Q.: Characterization of a highly cross-linked ultrahigh molecular-weight polyethylene in clinical use in total hip arthroplasty. *J. Arthroplasty* **23**, 751–761 (2008). <https://doi.org/10.1016/j.arth.2007.06.006>
- Oral, E., Christensen, S.D., Malhi, A.S., Wannomae, K.K., Muratoglu, O.K.: Wear resistance and mechanical properties of highly cross-linked, ultrahigh-molecular weight polyethylene doped with vitamin E. *J. Arthroplasty* **21**, 580–591 (2006). <https://doi.org/10.1016/j.arth.2005.07.009>
- Scemama, C., Anract, P., Dumaine, V., Babinet, A., Courpied, J.P., Hamadouche, M.: Does vitamin E-blended polyethylene reduce wear in primary total hip arthroplasty: a blinded randomised clinical trial. *Int. Orthop.* **41**, 1113–1118 (2017). <https://doi.org/10.1007/s00264-016-3320-2>
- Davidson, J.A.: Characteristics of metal and ceramic total hip bearing surfaces and their effect on long-term ultra high molecular weight polyethylene wear. *Clin. Orthop. Relat. Res.* **294**, 361–378 (1993)
- Ching, H.A., Choudhury, D., Nine, M.J., Abu Osman, N.A.: Effects of surface coating on reducing friction and wear of orthopaedic implants. *Sci. Technol. Adv. Mater.* **15**, 014402 (2014). <https://doi.org/10.1088/1468-6996/15/1/014402>
- Langhorn, J., Borjali, A., Hippensteel, E., Nelson, W., Raeymaekers, B.: Microtextured CoCrMo alloy for use in metal-on-polyethylene prosthetic joint bearings: Multi-directional wear and corrosion measurements. *Tribol. Int.* **124**, 178–183 (2018). <https://doi.org/10.1016/j.triboint.2018.04.007>
- Borjali, A., Monson, K., Raeymaekers, B.: Friction between a polyethylene pin and a microtextured CoCrMo disc, and its correlation to polyethylene wear, as a function of sliding velocity and contact pressure, in the context of metal-on-polyethylene prosthetic hip implants. *Tribol. Int.* **127**, 568–574 (2018). <https://doi.org/10.1016/j.triboint.2018.07.005>
- Borjali, A., Langhorn, J., Monson, K., Raeymaekers, B.: Using a patterned microtexture to reduce polyethylene wear in metal-on-polyethylene prosthetic bearing couples. *Wear* **392–393**, 77–83 (2017). <https://doi.org/10.1016/j.wear.2017.09.014>
- Wang, M., Zhang, C., Wang, X.: The wear behavior of textured steel sliding against polymers. *Materials (Basel)* **10**, 330 (2017). <https://doi.org/10.3390/ma10040330>
- López-Cervantes, A., Domínguez-López, I., Barceinas-Sánchez, J.D.O., García-García, A.L.: Effects of surface texturing on the performance of biocompatible UHMWPE as a bearing material during in vitro lubricated sliding/rolling motion. *J. Mech. Behav. Biomed. Mater.* **20**, 45–53 (2013). <https://doi.org/10.1016/j.jmbbm.2012.12.010>
- Ito, H., Kaneda, K., Yuhta, T., Nishimura, I., Yasuda, K., Matsuno, T.: Reduction of polyethylene wear by concave dimples on the frictional surface in artificial hip joints. *J. Arthroplasty* **15**, 332–338 (2000)
- Allen, Q., Raeymaekers, B.: Surface texturing of prosthetic hip implant bearing surfaces: a review. *J. Tribol.* **143**, 040801 (2021). <https://doi.org/10.1115/1.4048409>
- Allen, Q., Raeymaekers, B.: Maximizing the lubricant film thickness between a rigid microtextured and a smooth deformable surface in relative motion, using a soft elasto-hydrodynamic lubrication model. *J. Tribol.* **142**, 071802 (2020). <https://doi.org/10.1115/1.4046291>
- Su, B., Huang, L., Huang, W., Wang, X.: The load carrying capacity of textured sliding bearings with elastic deformation. *Tribol. Int.* **109**, 86–96 (2017). <https://doi.org/10.1016/j.triboint.2016.11.030>
- Shinkarenko, A., Kligerman, Y., Etsion, I.: The effect of surface texturing in soft elasto-hydrodynamic lubrication. *Tribol. Int.* **42**, 284–292 (2009). <https://doi.org/10.1016/j.triboint.2008.06.008>
- Dowson, D., Taylor, C.M.: Fundamental aspects of cavitation in bearings. In: Dowson, D., Godet, M., Taylor, C.M. (eds.) *Cavitation and related phenomena in lubrication*, Proceedings of the 1st Leeds-Lyon symposium on tribology, pp. 15–26. Mechanical Engineering Publications Limited, Leeds (1974)
- Sommerfeld, A.: The hydrodynamic theory of lubrication friction. *Zeitschrift für Angew. Math. und Phys.* **50**, 97–155 (1904)
- Gumbel, L.: *Monatsblätter Berlin Bezirksver.*, vol. 5, pp. 87–104. Verein Deutscher Ingenieure (VDI), Düsseldorf (1914)
- Swift, H.W.: The stability of lubricating films in journal bearings. *Minutes Proc. Inst. Civ. Eng.* **233**, 267–288 (1932)
- Stieber, W.: *Das Schwimmlager*. Verein Deutscher Ingenieure (VDI), Verlag, Berlin (1933)

34. Jakobsson, B., Floberg, L.: The finite journal bearing considering vaporization. Report no. 190. Transactions of Chalmers University of Technology in Guthenberg, Sweden (1957)
35. Olsson, K.-O.: Cavitation in dynamically loaded bearings. Report no. 308. Transactions of Chalmers University of Technology in Guthenberg, Sweden (1965)
36. Elrod, H.G., Adams, M.I.: A computer program for cavitation and starvation problems. In: Dowson, D., Godet, M., Taylor, C.M. (eds.) Cavitation and related phenomena in lubrication, proceedings of the 1st Leeds-Lyon symposium on tribology, pp. 37–41. Mechanical Engineering Publications Limited, Leeds (1974)
37. Elrod, H.G.: A cavitation algorithm. *J. Lubr. Technol.* **103**, 350–354 (1981)
38. Vijayaraghavan, D., Keith, T.G.J.: Development and evaluation of a cavitation algorithm. *Tribol. Trans.* **32**, 225–233 (1989)
39. Fesanghary, M., Khonsari, M.M.: A modification of the switch function in the Elrod cavitation algorithm. *J. Tribol.* **133**, 024501 (2011). <https://doi.org/10.1115/1.4003484>
40. Miraskari, M., Hemmati, F., Jalali, A., Alqaradawi, M.Y., Gadala, M.S.: A robust modification to the universal cavitation algorithm in journal bearings. *J. Tribol.* **139**, 031703 (2017). <https://doi.org/10.1115/1.4034244>
41. Woloszynski, T., Podsiadlo, P., Stachowiak, G.W.: Efficient solution to the cavitation problem in hydrodynamic lubrication. *Tribol. Lett.* **58**, 18 (2015). <https://doi.org/10.1007/s11249-015-0487-4>
42. Biboulet, N., Lubrecht, A.A.: Efficient solver implementation for Reynolds equation with mass-conserving cavitation. *Tribol. Int.* **118**, 295–300 (2018). <https://doi.org/10.1016/j.triboint.2017.10.008>
43. Mezzadri, F., Galligani, E.: An inexact Newton method for solving complementarity problems in hydrodynamic lubrication. *Calcolo* **55**, 1 (2018)
44. Giacopini, M., Fowell, M.T., Dini, D., Strozzi, A.: A mass-conserving complementarity formulation to study lubricant films in the presence of cavitation. *J. Tribol.* **132**, 041702 (2010). <https://doi.org/10.1115/1.4002215>
45. Coyne, J.C., Elrod, H.G.: Conditions for the rupture of a lubricating film. Part I: Theoretical model. *J. Lubr. Technol.* **92**, 451–456 (1970). <https://doi.org/10.1115/1.3451441>
46. Coyne, J.C., Elrod, H.G.: Conditions for the rupture of a lubricating film- Part II New boundary conditions for Reynolds equation. *J. Lubr. Technol.* **93**, 156–167 (1971). <https://doi.org/10.1115/1.3451506>
47. Song, Y., Gu, C., Ren, X.: Development and validation of a gaseous cavitation model for hydrodynamic lubrication. *Proc. Inst. Mech. Eng. J.* **229**, 1227–1238 (2015). <https://doi.org/10.1177/1350650115576247>
48. Hirayama, T., Sakurai, T., Yabe, H.: A theoretical analysis considering cavitation occurrence in oil-lubricated spiral-grooved journal bearings with experimental verification. *J. Tribol.* **126**, 490–498 (2004). <https://doi.org/10.1115/1.1691436>
49. Bayada, G., Chupin, L.: Compressible fluid model for hydrodynamic lubrication cavitation. *J. Tribol.* **135**, 041702 (2013). <https://doi.org/10.1115/1.4024298>
50. Bayada, G.: From a compressible fluid model to new mass conserving cavitation algorithms. *Tribol. Int.* **71**, 38–49 (2014). <https://doi.org/10.1016/j.triboint.2013.10.014>
51. Etsion, I., Ludwig, L.P.: Observation of pressure variation in the cavitation region of submerged journal bearings. *J. Lubr. Technol.* **104**, 157–163 (1982)
52. Liu, H., Xu, H., Ellison, P.J., Jin, Z.: Application of computational fluid dynamics and fluid-structure interaction method to the lubrication study of a rotor-bearing system. *Tribol. Lett.* **38**, 325–336 (2010). <https://doi.org/10.1007/s11249-010-9612-6>
53. Ausas, R., Ragot, P., Leiva, J., Jai, M., Bayada, G., Buscaglia, G.C.: The impact of the cavitation model in the analysis of microtextured lubricated journal bearings. *J. Tribol.* **129**, 868–875 (2007). <https://doi.org/10.1115/1.2768088>
54. Zhang, J., Meng, Y.: Direct observation of cavitation phenomenon and hydrodynamic lubrication analysis of textured surfaces. *Tribol. Lett.* **46**, 147–158 (2012). <https://doi.org/10.1007/s11249-012-9935-6>
55. Wang, L., Wang, W., Wang, H., Ma, T., Hu, Y.: Numerical analysis on the factors affecting the hydrodynamic performance for the parallel surfaces with microtextures. *J. Tribol.* **136**, 021702 (2014). <https://doi.org/10.1115/1.4026060>
56. Qiu, Y., Khonsari, M.M.: On the prediction of cavitation in dimples using a mass-conservative algorithm. *J. Tribol.* **131**, 041702 (2009). <https://doi.org/10.1115/1.3176994>
57. Dobrica, M.B., Fillon, M., Pascovici, M.D., Cicone, T.: Optimizing surface texture for hydrodynamic lubricated contacts using a mass-conserving numerical approach. *Proc. Inst. Mech. Eng. J* **224**, 737–750 (2010)
58. Jagatia, M., Jin, Z.M.: Analysis of elastohydrodynamic lubrication in a novel metal-on-metal hip joint replacement. *Proc. Inst. Mech. Eng. H* **216**, 185–193 (2002)
59. Qiu, M., Chyr, A., Sanders, A.P., Raeymaekers, B.: Designing prosthetic knee joints with bio-inspired bearing surfaces. *Tribol. Int.* **77**, 106–110 (2014). <https://doi.org/10.1016/j.triboint.2014.04.025>
60. Chyr, A., Qiu, M., Speltz, J.W., Jacobsen, R.L., Sanders, A.P., Raeymaekers, B.: A patterned microtexture to reduce friction and increase longevity of prosthetic hip joints. *Wear* **315**, 51–57 (2014). <https://doi.org/10.1016/j.wear.2014.04.001>
61. Venner, C.H., Lubrecht, A.A.: *Multilevel methods in lubrication*. Elsevier, New York (2000)
62. Bergström, J.S., Kurtz, S.M., Rimnac, C.M., Edidin, A.A.: Constitutive modeling of ultra-high molecular weight polyethylene under large-deformation and cyclic loading conditions. *Biomaterials* **23**, 2329–2343 (2002). [https://doi.org/10.1016/S0142-9612\(01\)00367-2](https://doi.org/10.1016/S0142-9612(01)00367-2)
63. Wang, F.C., Jin, Z.M.: Elastohydrodynamic lubrication modeling of artificial hip joints under steady-state conditions. *J. Tribol.* **127**, 729–739 (2005). <https://doi.org/10.1115/1.1924460>
64. Saikko, V.: Effect of contact pressure on wear and friction of ultra-high molecular weight polyethylene in multidirectional sliding. *Proc. Inst. Mech. Eng. H* **220**, 723–731 (2006)
65. Grollman, A.: The vapor pressure of dog's blood at body temperature. *J. Gen. Physiol.* (1928). <https://doi.org/10.1017/CBO9781107415324.004>
66. Malik, S., Kakoty, S.K.: Analysis of dimple textured parallel and inclined slider bearing. *Proc. Inst. Mech. Eng. J* **228**, 1343–1357 (2014). <https://doi.org/10.1177/1350650114538779>
67. Nečas, D., Usami, H., Niimi, T., Sawae, Y., Krupka, I., Hartl, M.: Running-in friction of hip joint replacements can be significantly reduced: the effect of surface-textured acetabular cup. *Friction* **8**, 1137–1152 (2020). <https://doi.org/10.1007/s40544-019-0351-x>
68. Allen, Q., Raeymaekers, B.: The effect of texture floor profile on the lubricant film thickness in a textured hard-on-soft bearing with relevance to prosthetic hip implants. *J. Tribol.* **143**, 021801 (2021). <https://doi.org/10.1115/1.4047753>
69. Codrignani, A., Frohnapfel, B., Magagnato, F., Schreiber, P., Schneider, J., Gumbsch, P.: Numerical and experimental investigation of texture shape and position in the macroscopic contact. *Tribol. Int.* **122**, 46–57 (2018). <https://doi.org/10.1016/j.triboint.2018.02.001>
70. Jalali-Vahid, D., Jagatia, M., Jin, Z.M., Dowson, D.: Prediction of lubricating film thickness in UHMWPE hip joint replacements. *J. Biomech.* **34**, 261–266 (2001). [https://doi.org/10.1016/S0021-9290\(00\)00181-0](https://doi.org/10.1016/S0021-9290(00)00181-0)
71. Gao, L., Dowson, D., Hewson, R.W.: A numerical study of non-Newtonian transient elastohydrodynamic lubrication of

- metal-on-metal hip prostheses. *Tribol. Int.* **93**, 486–494 (2016). <https://doi.org/10.1016/j.triboint.2015.03.003>
72. Nečas, D., Vrbka, M., Galandakova, A., Kfupka, I., Hartl, M.: On the observation of lubrication mechanisms within hip joint replacements. Part I: Hard-on-soft bearing pairs. *J. Mech. Behav. Biomed. Mater.* **89**, 237–248 (2019). <https://doi.org/10.1016/j.jmbbm.2018.09.022>
73. Zhang, H., Hua, M., Dong, G.N., Zhang, D.Y., Chin, K.S.: A mixed lubrication model for studying tribological behaviors of surface texturing. *Tribol. Int.* **93**, 583–592 (2016). <https://doi.org/10.1016/j.triboint.2015.03.027>
74. Myant, C., Cann, P.: In contact observation of model synovial fluid lubricating mechanisms. *Tribol. Int.* **63**, 97–104 (2013). <https://doi.org/10.1016/j.triboint.2012.04.029>
75. Qiu, M., Raeymaekers, B.: The load-carrying capacity and friction coefficient of incompressible textured parallel slider bearings with surface roughness inside the texture features. *Proc. Inst. Mech. Eng. J* **229**, 547–556 (2015). <https://doi.org/10.1177/1350650114545352>

Publisher's Note Springer Nature remains neutral with regard to jurisdictional claims in published maps and institutional affiliations.